High Figure-of-Merit Gallium Oxide UV Photodetector on Silicon by Molecular Beam Epitaxy: A Path toward Monolithic Integration

Partha Mukhopadhyay,* Isa Hatipoglu, Tamil Selvan Sakthivel, Daniel A. Hunter, Paul R. Edwards, Robert W. Martin, Gunasekar Naresh-Kumar, Sudipta Seal, and Winston V. Schoenfeld

A high figure-of-merit UV-C solar-blind photodetector (PD) fabricated from thin-film beta-gallium oxide (β-Ga$_2$O$_3$) grown on *n*-Si substrates by plasma-assisted molecular beam epitaxy is demonstrated. Film growth sequences for nucleation of Ga$_2$O$_3$ on (100)- and (111)-oriented Si substrates are developed, and the influence of crucial growth parameters is systematically investigated, namely, substrate temperature, oxygen flow rate, and plasma power on the functional properties of the PDs. The PDs show an ultra-high responsivity of 837 A W^{-1} and a fast ON/OFF time below 4 ms at -5 V. In addition, they display strong rectifying properties and a sharp cutoff below 280 nm with the average responsivities between 10 and 80 A W^{-1}, a detectivity on the order of 10^{10} Jones, and rise/fall times between 4 and 500 ms. High photoconductive gain is likely to be due to the mid-bandgap donor/acceptor defect levels, including oxygen vacancies in the form of self-trapped holes. It is demonstrated that these defect levels can be modified by controlling the growth conditions, thereby allowing for tailoring of the PD characteristics for specific applications. The methodology represents a cost-effective solution over homoepitaxial approaches, with characteristics that meet or exceed those reported previously, offering new possibilities for on-wafer integration with Si opto-electronics.

1. Introduction

Detection in the UV-C spectral region with a cutoff wavelength below $\approx$280 nm, i.e., solar blind is of great interest and has numerous potential applications in field, including military defense, UV astronomy, non-line-of-sight short-range communications, flame sensing, and environment and safety monitoring such as air/water purification.[1] With a wide bandgap of $\approx$4.7–4.9 eV and excellent chemical and physical stability, gallium oxide (Ga$_2$O$_3$) has become an attractive choice of material for UV-C photodetectors (PDs).[2] The unique combination of high bandgap and ability to extrinsically *n*-type-doped Ga$_2$O$_3$ has led to a measurable interest in studying a wide range of prospective heterostructure combinations, such as MgZnO/Ga$_2$O$_3$,[3] Ga$_2$O$_3$/GaN,[4] Ga$_2$O$_3$/SiC,[5] and Ga$_2$O$_3$/Si,[6–14] for use as UV PDs. Among these heterojunctions, Ga$_2$O$_3$/Si is especially attractive due to the well-known cost and availability advantages of Si substrates, and its prominent applications in Si-based optoelectronic integrated circuits.

Dr. P. Mukhopadhyay, I. Hatipoglu, Prof. W. V. Schoenfeld
CREOL
The College of Optics and Photonics
University of Central Florida
4000 Central Florida Blvd, Orlando, FL 32816, USA
E-mail: partha.mukhopadhyay@creol.ucf.edu

Dr. T. S. Sakthivel, Prof. S. Seal, Prof. W. V. Schoenfeld
Department of Material Science and Engineering
University of Central Florida
4000 Central Florida Blvd, Orlando, FL 32816, USA

Ⓘ The ORCID identification number(s) for the author(s) of this article can be found under https://doi.org/10.1002/adpr.202000067.

D. A. Hunter, Dr. P. R. Edwards, Prof. R. W. Martin, Dr. G. Naresh-Kumar
Department of Physics
SUPA
University of Strathclyde
Glasgow G4 0NG, UK

Prof. S. Seal
NanoScience Technology Center
University of Central Florida
4000 Central Florida Blvd, Orlando, FL 32816, USA

Prof. S. Seal
College of Medicine
University of Central Florida
4000 Central Florida Blvd, Orlando, FL 32816, USA

Prof. W. V. Schoenfeld
Department of Electrical and Computer Engineering
University of Central Florida
4000 Central Florida Blvd, Orlando, FL 32816, USA

Ga_2O_3 and its related alloyed compounds have been studied extensively for lateral and vertical Schottky PDs on sapphire and bulk Ga_2O_3 substrates. However, there are very few reports on the growth of Ga_2O_3 on Si substrates[12–15] with detailed experimental data on heterointerface band alignment between Ga_2O_3 and Si. To the best of our knowledge, there is no reported work on UV-C PDs fabricated from plasma-assisted molecular beam epitaxy (PAMBE) β-Ga_2O_3 grown on n-type Si substrate, the novelty of this work. To date, pulsed layer deposition (PLD) has been a popular choice for Ga_2O_3/Si.[6–8,13] Besides PLD, β-Ga_2O_3 has also been deposited using a seed layer transfer technique on Si,[9] achieving high responsivity and low dark current, however, at zero bias only as self-powered lateral metal–semiconductor–metal (MSM) solar-blind PD. n-type β-Ga_2O_3 nanobelts contacted onto p-Si substrate have also been explored for UV-C PDs.[10] Amorphous Ga_2O_3-based PDs have also been demonstrated on silicon substrates using atomic layer deposition (ALD)[11,12,14] and metal–organic chemical vapor deposition (MOCVD).[15]

Albeit Ga_2O_3/Si PDs have been demonstrated by the growth methods mentioned earlier, none investigate the influence of growth conditions on material properties, starting from the nucleation layers, and their impact on the functional properties of the fabricated devices, the objective of this work. In this article, we introduce heteroepitaxial MBE growth approaches to combine different figure-of-merits for producing UV-C PDs. We performed a range of growth optimization experiments to understand the impact of growth conditions on the nucleation and subsequent growth of polycrystalline Ga_2O_3 film on lattice-mismatched n-type silicon (100)- and (111)-oriented substrates. In particular, we vary the Ga pre-deposition, growth temperature, oxygen flow, and plasma power. We then analyzed the structural and optical properties of the grown samples and, subsequently, fabricated the PDs to understand their functional properties. This systematic approach of relating the growth conditions to the device properties provides useful guidance for researchers working in this growing field of manufacturing UV-C PDs.

2. Experimental Section

Ga_2O_3 epilayers were grown by PAMBE on n-type (100) and (111) silicon substrates. Oxygen was supplied by an SVT Associates Inc. plasma source, and a standard Knudsen effusion cell was used to source the Ga. Prior to the growth, the Si substrates were cleaned using an internally developed process of multiple cycles of ozone and dilute hydrofluoric acid, followed by a deionized water rinse, removing surface contamination and forming a thin high-quality SiO_2 surface layer. The substrate was then thermally cleaned at high temperature (800 °C) under vacuum ($\approx 1 \times 10^{-9}$ Torr) inside the MBE chamber for several hours to remove the SiO_2 surface layer and ensure the high crystalline quality of the underlying Si substrate. Further surface cleaning was performed by a Ga treatment, as described elsewhere.[16] In situ reflection high energy electron diffraction (RHEED) reconstruction patterns were used to confirm the complete removal of SiO_2 from the surface. Prior to opening the MBE oxygen plasma shutter, metallic Ga was pre-deposited for several minutes to form a thin layer of Ga at a substrate temperature of 500 °C. After this low temperature nucleation of Ga_2O_3, the substrate temperature (T_{sub}) was ramped up to 660–730 °C. When the target growth temperature was reached, a 2 min anneal was carried out before the growth to improve the crystalline quality of the nucleation layer, as verified by RHEED. Next, a thick Ga_2O_3 layer was grown at a typical chamber pressure of 1.5–2.0×10^{-5} Torr. Further annealing was carried out after the growth under low oxygen flow rate inside the MBE, and the samples were then cooled down using a slow T_{sub} reduction rate to avoid cracking of the film due to the thermal expansion coefficient mismatch between Ga_2O_3 and Si. The average thickness of the Ga_2O_3 films was ≈ 250 nm, measured by profilometry at the step edge between the film and the area covered by the molybdenum platen. **Table 1** summarizes the growth conditions and device characteristics of all 12 samples used in this study.

Structural properties were examined by conventional omega–2Theta (ω–2θ) powder scan X-ray diffraction (XRD) using a PANalytical X'Pert Cu-K$_{\alpha 1}$ beam ($\lambda = 1.5405$ Å). Electron

Table 1. Summary of growth conditions and device characteristics of samples.

Sample	Si substrate	O_2 flow [sccm]	T_{sub} [°C]	Plasma power [W]	Rise time, τ_{1r} [ms]	Fall time, τ_{1f} [ms]	Peak responsivity [A W^{-1}]	Detectivity [$\times 10^{10}$ Jones]
A1	(100)	1.6	700	300	–	–	–	–
A2	(100)	2.0	700	300	<4	<4	0.04 (@0 V)	–
A3	(100)	2.5	700	300	–	–	3.3	1.14
B1	(111)	1.6	700	300	–	–	–	–
B2	(111)	2.0	700	300	<4	<4	0.06 (@0 V)	0.009
B3	(111)	2.5	700	300	70	85	13.2	3.07
B4	(111)	2.5	730	300	287	174	15.8	3.37
C1	(111)	2.5	660	300	2400	880	837	28.1
C1A	(111)	2.5	660	300	540	440	79.1	8.84
C2	(111)	2.5	700	325	281	291	26.4	5.06
C3	(111)	2.5	700	350	353	326	66.8	10.1
C4	(111)	2.5	730	350	≈ 4	55	11.3	1.2

backscatter diffraction (EBSD) was also performed to understand the crystallographic orientation of the Ga_2O_3 film grown on lattice mismatched Si substrate. The surface morphology was analyzed by imaging backscattered electrons in a JEOL JXA-8530F field-emission electron probe micro-analyzer (EPMA). In addition to this, atomic force microscopy (AFM) was also performed for estimating the root mean square (RMS) surface roughness on a $5 \times 5 \mu m^2$ scanned area. To study the optical properties and elemental composition, we performed room temperature (RT) cathodoluminescence (CL) spectroscopy and wavelength dispersive X-ray spectroscopy (WDS), respectively, in the EPMA. Both the CL and WDS spectra were obtained for the samples grown on (111)-oriented Si substrates with an electron beam energy of 4 kV and a beam current of 40 nA. The CL spectra were acquired by a spectrometer with a focal length of 163 mm with 300 grooves mm^{-1} grating blazed at 500 nm, a 105 μm entrance slit (fiber size), and a 1024-element charge-coupled device.

X-ray photoelectron spectroscopy (XPS) measurements were performed using an ESCALAB-250Xi spectrometer at RT in ultra-high vacuum (UHV), below 7×10^{-9} mbar. The system is fitted with a monochromatic Al-K_α radiation source, operating at a power of 300 W (15 kV, 20 mA), and the spot size of the beam was 650 μm. The carbon (C 1s) peak at 284.6 eV was used as a reference for calibration. Thermo Avantage software was utilized for deconvolution to identify the nature of elements present in samples. Spectra were fitted with a Gaussian–Lorentzian peak shape after the subtraction of a smart background. To ensure proper peak fitting, spectra were analyzed using an automated incremental peak deconvolution program, which varied the peak height within an envelope over a complete range to determine the best fit, and checked using the ϕ-squared value to the actual data.

Vertical Schottky PDs (500 μm diameter) were fabricated from the Ga_2O_3 epilayers using the standard photolithography methods. Ti/Au (20/100 nm) was deposited on the backside of Si substrate and annealed at 400 °C for 5 min to form an ohmic contact.[17] The front-side Schottky contact was formed with two steps accomplished with a standard liftoff procedure: 1) deposition of a high work function ($\Phi_m \approx 5.5$ eV) semitransparent layer of Pt (≈ 3 nm), and 2) subsequent deposition of a thick Ni/Au ring contact to aid in physical probing of the device. The schematic of the fabricated device is shown in **Figure 1**. The thin Pt semitransparent contact enables light transmission from the top

side of the device ($\approx 50\%$ at 240 nm) while still creating a suitable Schottky contact across the illuminated active region of the device. The current–voltage (I–V) and temporal characteristics of the Schottky PDs were measured with a Keithley 2450 source-meter unit (SMU) using probe tips to contact specific devices on the sample surface. Spectral responsivity was measured using a Newport MS257 UV–vis monochromator fitted with a 30 W deuterium lamp. Light incident on the device was measured using a calibrated Si photodiode to enable absolute responsivity values to be determined.

3. Results and Discussion

Thin-film growth of lattice mismatch materials largely depends on the nucleation technique. In particular, vertical type devices, such as the PDs presented here, depend highly on the crystalline quality at the heterointerface. Thus, we have examined various PAMBE nucleation growth techniques to nucleate Ga_2O_3 on (100)- and (111)-oriented-doped Si substrates and studied the functional properties of the grown material and the fabricated device characteristics.

3.1. Nucleation on Lattice Mismatch Si Substrate

Prior to investigating the impact of various growth conditions on the Ga_2O_3/Si heterostructures, we investigated the role of Ga and oxygen on the nucleation of the Ga_2O_3 epilayers. More specifically, we investigated Ga pre-deposition first to avoid amorphous SiO_2 formation.

3.1.1. Ga Pre-Deposition

Our earlier work demonstrated that the sticking coefficient of Ga on Si is rather weak, and at several hundreds of °C, Ga is quite volatile.[18] Thus, we chose to use a low-temperature Ga pre-deposition to ensure the formation of a Ga_2O_3 seed layer before increasing the substrate temperature for the growth of the Ga_2O_3 epilayers. Ga was pre-deposited on the Si substrate at 500 °C before initializing and opening the oxygen plasma shutter to fully cover the substrate surface. We found this a critical step to avoid the formation of amorphous SiO_x at the Ga_2O_3/Si interface. We observed that shorter pre-deposition time (≈ 5 min) led to inadequate Ga coverage on the Si substrate. To explore this further, we carried out XPS to quantitatively identify the presence of chemical compounds on the surface of this sample.

The XPS survey of the sample grown under inadequate Ga pre-deposition showed that the surface contains C, O, Ga, and Si as the primary elements, as shown in **Figure 2**a (blue color). The quantified atomic percentage from XPS (C 1s = 14.29%, Ga 3d = 2.03%, Si 2s = 29.51%, and O 1s = 54.17%) indicates that the presence of Ga on the surface is very low compared with Si. Fitting of O 1s region, in Figure 2d, shows two peaks, centered at 531.1 eV (Ga_2O_3—10.98%)[19] and 532.8 eV (SiO_2—89.02%), confirming the dominant presence of Si on the top surface in the form of SiO_2. In addition, the Si 2p region in Figure 2b clearly indicates that the Si is highly oxidized and present in the form of SiO_2 on the surface, whereas Figure 2c elaborates the Ga 3d to show the presence of gallium in the form of Ga_2O_3 as a single
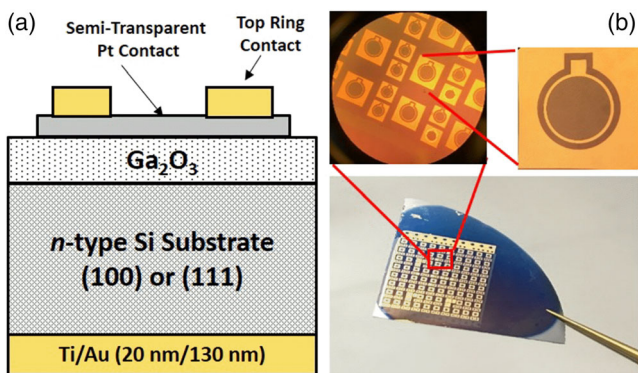
Figure 1. a) Ga_2O_3/Si Schottky device cross-sectional schematic. b) Photograph of fabricated devices.
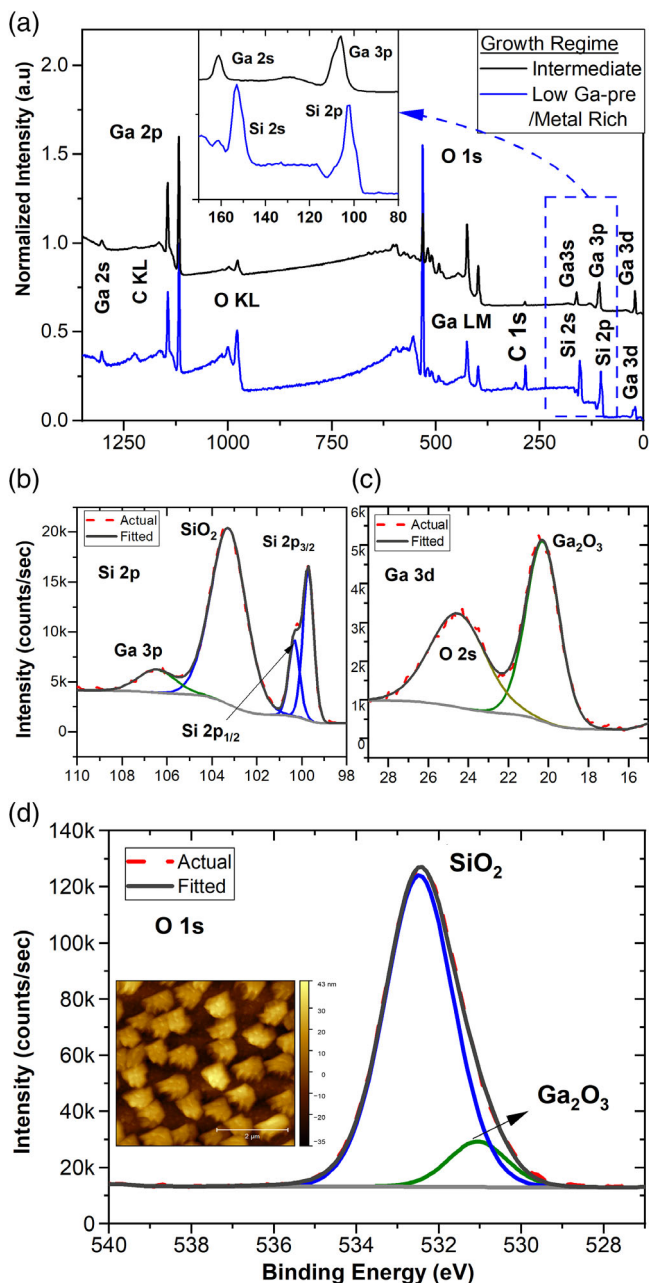
Figure 2. a) XPS spectra normalized intensity survey spectra for samples grown under different regimes, and (inset) zoomed area illustrates different peak positions. Selective XPS spectral line of B1 sample: b) deconvoluted and fitted Si 2p spectrum shows the presence of both Si and SiO_2 due to the lack of Ga atoms on the surface, c) deconvoluted and fitted XPS spectral lines of Ga 3d, and d) deconvoluted and fitted O 1s spectral emission from B1 sample showing the mixed compounds of SiO_2 and Ga_2O_3. Inset is a $5 \times 5\ \mu m^2$ typical AFM surface topography of the metal-rich sample, which shows the clustering nature with high surface roughness.

component. The concentration of surface SiO_2 and Ga_2O_3, as shown in Figure 2d, was calculated from the ratio of the integrated areas of the XPS O 1s peak related to SiO_2 or Ga_2O_3 to the total integral area of the entire O 1s region.

This result shows that the amorphous SiO_2 is forming at the substrate/epilayer interface during nucleation due to lack of sufficient surface covering by Ga atoms. In addition, we did not observe any Ga_2O_3 XRD ω–2θ peaks (not shown here) from the epilayer, further confirming SiO_2 as the primary compound present in the nucleation layer.

The AFM topographic image in the inset of Figure 2d shows the clustering nature, which further supports our claim of the coexistence of SiO_2 and Ga_2O_3 side-by-side. This, in turn, leads to a highly defective interface and the lack of observable photoresponse in the fabricated PDs based on such epilayers. Notably, we observed the same phenomena for both (100) and (111) orientations of the Si substrate.

We also analyzed the RHHED pattern and their intensities to understand the role of Ga pre-deposition. We found that the Ga pre-deposition of $\approx$10 min was sufficient to cover the wafer surface before nucleation, evident from the full transition of the silicon substrate RHEED pattern to the dimming intensity from Ga-coated surface. We further monitored the RHEED pattern upon oxygen plasma supply for the nucleation of Ga_2O_3, verifying suitable nucleation as the RHEED shifted to that of a crystalline Ga_2O_3 layer. Having identified the importance of Ga pre-deposition, all further film growth reported in this manuscript utilized a 10 min pre-deposition of Ga at 500 °C before initiating oxygen supply and the thin film growth.

3.1.2. Role of Oxygen Flux

With a proper Ga pre-deposition process identified, we then investigated the role of oxygen flow rate at 1.6, 2.0, and 2.5 sccm on both (100) and (111) Si substrates. With the lowest oxygen flow of 1.6 sccm, samples A1 and B1 had no observable XRD peak for Ga_2O_3, irrespective of substrate orientation, with only the Si (400) or (111) substrate peak present, as shown in **Figure 3**. Based on prior work, this is likely due to growth under metal-rich conditions where the formation of gallium sub-oxides, specifically Ga_2O, leads limited or no growth of Ga_2O_3.[20,21]
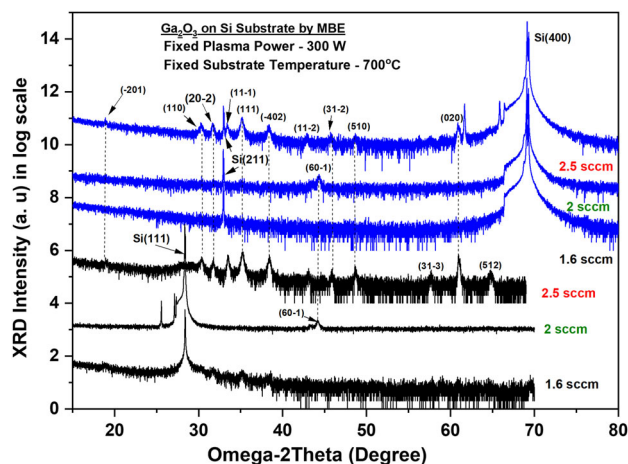
Figure 3. XRD of samples grown on both the (100) and (111) orientations in blue and black color, respectively, under varying oxygen flow rate of 1.6, 2.0, and 2.5 sccm while fixing the plasma power and substrate temperature.

**ADVANCED
SCIENCE NEWS**

www.advancedsciencenews.com

**ADVANCED
PHOTONICS
RESEARCH**
Open Access

www.adpr-journal.com

Ga_2O is a volatile gaseous compound and does not incorporate into the epitaxial film, consuming the available Ga at the growth surface and leading to the lack of significant Ga_2O_3 epitaxy. Interestingly, upon increasing oxygen flux keeping the Ga flux same, we observed the presence of Ga_2O_3 in the epilayers.

To investigate the surface chemical composition further, we performed XPS on the 1.6 sccm samples (A1 and B1) grown on both the substrate orientations. Interestingly, XPS shows the presence of a high percentage of Si in the form of SiO_2, quite similar to the results shown in Figure 2 for sample B1 with Ga-deficient pre-deposition. More than 80% oxygen is bonded with Si and present on the surface as SiO_2, similar to that shown in Figure 2d. This further supports our hypothesis of competition for active oxygen atoms by Ga and Si at the interface during nucleation. Lower oxygen supply promotes metal-rich growth conditions, leading to greater formation of volatile Ga_2O rather than stable Ga_2O_3. This, in conjunction with the strong tendency for Si to bond with oxygen, leads to the presence of SiO_2 and limited Ga_2O_3. We have previously observed a similar phenomenon during the growth of AlGaN with insufficient nitrogen flux supply in MBE, promoting the formation of AlN instead of AlGaN despite supplying sufficient Ga flux.[16]

3.2. Impact of O_2 Flow Rate on the Growth of Ga_2O_3 Epilayer

Carrying out the nucleation and growth process at a higher oxygen flow rate of 2.0 and 2.5 sccm results in an observable Ga_2O_3 epilayer on Si substrate under fixed Ga flux. To further investigate the growth regime, the oxygen flow rate variation experiment was done using a 300 W plasma power and a T_{sub} of 500 °C at nucleation, followed by the subsequent high-temperature Ga_2O_3 growth at 700 °C. The chosen oxygen flow rate for each sample was maintained for both the nucleation and the high temperature growth. The 2.0 sccm sample results weak single peak in the XRD at 44.38° in Figure 3, attributable to that for (60−1) monoclinic Ga_2O_3[7] on both (100) and (111) Si substrates (samples A2 and B2, respectively). Interestingly, no other XRD peaks for Ga_2O_3 are present. In contrast, when increasing to 2.5 sccm for nucleation (samples A3 and B3), we observe a significant number of Ga_2O_3 peaks in the XRD scans for both substrate orientations, as shown in Figure 3. It depicts the polycrystalline nature of the monoclinic phase of Ga_2O_3 film on the Si substrate. To support the XRD measurements, we also performed EBSD mapping, confirming the same polycrystalline nature of the samples. Both the [010] and [−201] were clearly seen in EBSD images (not shown here) in addition to other orientations.

Collectively, the XRD ω–2θ powder scan in Figure 3 suggests that there is little dependence of the crystalline nature of the Ga_2O_3 epilayers on substrate orientation, irrespective of oxygen flow rate. While XRD data alone cannot determine the expected performance of resultant UV detectors from the epilayers, we can conclude that a minimum oxygen flow (2.0 sccm in our case) is required for successful nucleation and growth of crystalline Ga_2O_3 suitable for UV detectors. Notably, XPS surveys for both samples (O_2 flow of 2.0 and 2.5 sccm) show an absence of Si on the grown polycrystalline film. Occurrence of Si 2s–2p and Ga 2s–3p from layers with and without SiO_2, respectively, is shown

in inset of Figure 2a. The intermediate in Figure 2a referred to the 2.5 sccm growth (sample B3). Thus, we conclude that the oxygen flows of 2.0 sccm and above lead to growth under less Ga-rich conditions where the formation of Ga_2O is sufficiently suppressed to allow for successful nucleation and growth of Ga_2O_3 on the Si substrate. As noted earlier (see Section 3.1.2), we attribute the lack of clear XRD peaks in the 1.6 sccm samples (A1 and B1) to the formation of SiO_2 that leads to reduced or minimal Ga_2O_3 growth as a result of the volatile Ga_2O formation, as supported by the XPS data.

3.3. Impact of Substrate Temperature and Plasma Power on the Growth of Ga_2O_3 Epilayer

Having identified a suitable intermediate growth regime at the oxygen flow rates of 2.5 sccm, we studied the impact of substrate temperature on the epilayers. **Figure 4** shows the ω–2θ XRD scan for samples grown under varying T_{sub} and plasma power while oxygen flow rate was held constant at 2.5 sccm.

Samples (B3 and C1) grown under 300 W plasma-power, using the substrate temperatures of 660 and 700 °C, result in no observable difference in the crystalline quality as measured by XRD. However, at the higher T_{sub} of 730 °C (sample B4), the XRD is considerably different, with only a single Ga_2O_3 related peak at 44.38°, associated with the (60−1) plane from monoclinic Ga_2O_3. Using the same T_{sub} of 730 °C but increasing the plasma power from 300 to 350 W results in XRD with multiple Ga_2O_3 peaks from the epilayer (sample C4 in Figure 4). Interestingly, when plasma power increased from 300 to 350 W for T_{sub} of 730 °C (sample C4), the XRD shows similar multiple peaks to that of sample B3 (300 W/700 °C).

To better understand this observation, we considered the growth rates for each of these conditions, as shown in **Figure 5**. For the substrate temperatures of 700 and 730 °C, increasing plasma power results in an increase in growth rate. In particular, for a T_{sub} of 700 °C, increasing the plasma power from 300 to 350 W results in a systematic increase of growth rate from 30 to 66 nm h^{-1}. Similarly, at a T_{sub} of 730 °C, a plasma power increase leads to a rise in growth rate from 26 to 33 nm h^{-1},
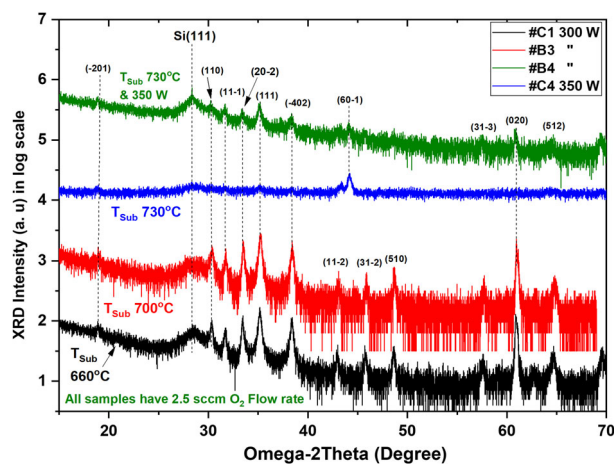
Figure 4. XRD for samples grown under varying substrate temperature and oxygen plasma power.

**ADVANCED
SCIENCE NEWS**

www.advancedsciencenews.com

**ADVANCED
PHOTONICS
RESEARCH**
Open Access

www.adpr-journal.com
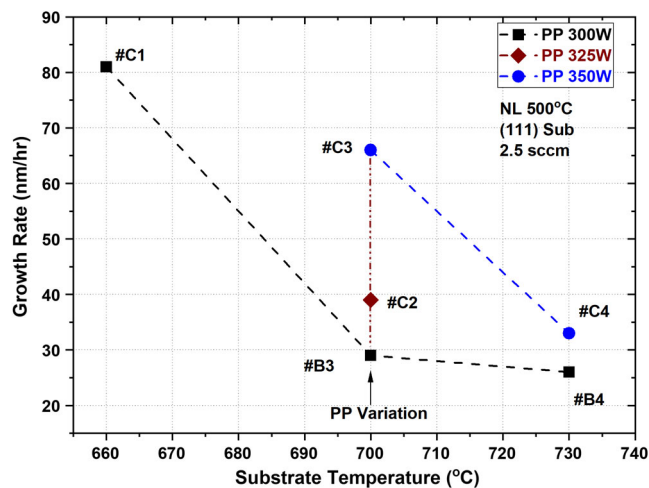
Figure 5. Growth rate variation under different substrate temperature and plasma power.

Figure 6. RT representative CL spectra from samples grown under 2.5 sccm O_2 and inset is energy levels corresponding to different defects. The blue and black spectrum is obtained with a center wavelength of 428 and 700 nm, respectively.

though the increase is not as substantial. As we are growing in metal-rich conditions, the observed increase in growth rate is likely due to a reduction in the formation of volatile Ga_2O at higher plasma powers, leading to an increased formation of Ga_2O_3.[21]

3.3.1. Surface Morphology of the Thin-film

The surface morphology plays a key role on the device processing steps. To understand the surface morphology, secondary and back-scattered electron images were acquired (see Figure S1, Supporting Information). These images provide insight into the effect of varying the growth parameters on the surface morphology of the grown epilayers. Increasing T_{sub} without increasing plasma power has a pronounced effect on the topography of the B4 sample. It has finer grains compared with the coarser grains in the B3 sample grown at a lower T_{sub} of 700 °C. Interestingly, when the plasma power increased from 300 to 350 W for a T_{sub} of 730 °C (sample C4), the topography seems to recover back to that of sample B3 (300 W/700 °C). AFM images (see Figure S2, Supporting Information) shows similar topography too. Additional investigation with high-resolution transmission electron microscopy is necessarily better to understand the nanoscale structural changes and source of this behavior.

3.4. Optical Characterization by CL Spectroscopy

Prior literature on the RT photoluminescence (PL)[22,23] and CL[24,25] measurements of Ga_2O_3 epilayers indicates the presence of donor levels in the bandgap due to defects in the form of oxygen vacancy, Ga vacancy, and unintentional doping generated due to the growth limitations. We have observed similar characteristics in RT CL measurements of our Ga_2O_3 film grown on Si substrates, suggesting that our films follow the nature of their homoepitaxial counterparts.

The characteristics of CL spectra (sample B3) in **Figure 6** show emission bands centered approximately at 360 nm (3.5 eV),
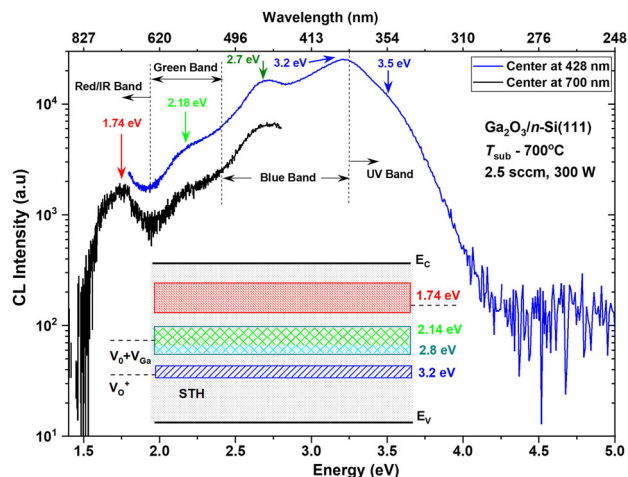
390 nm (3.20 eV), 460 nm (2.70 eV), 570 nm (2.17 eV), and 710 nm (1.74 eV). At RT, blue band intensity is much stronger than UV, green, and red/near IR band. We notice that green emission is the weakest one among all other bands. We do not observe any near band edge emission (NBE recombination of electrons and holes) in our samples. These emission bands are due to defects that introduce energy levels within the bandgap, typically behaving as a deep or shallow donor, as shown in the inset of Figure 6. They play a crucial role in modifying the carrier recombination as well as conductivity of the film, thereby influencing the peak responsivity, detectivity, spectral, and transient behavior of resultant PDs. We further investigated the impact of growth parameters on the occurrence of these defects in view of device characteristics discussed in the later section (Section 3.5.6–3.5.8). Notably, the peak positions of UV, blue, green, and red emission were almost independent of growth temperature and plasma power.

The broad UV and part of blue emission is intrinsic in nature, and it is widely attributed to the recombination of free electrons and self-trapped holes (STHs)[22–24,26–28] or the recombination of free electrons with self-trapped excitons (STEs). A hole in the valence band causes a local distortion to the electric field, rendering it immobile, i.e., self-trapped, hence the name STH. When electrons or holes have a strong coupling to the crystal lattice, a carrier may be self-trapped (for, e.g., a polaron) in its own lattice field. Interaction of such a carrier to a bound electron hole pair (exciton) is commonly described as an STE. These STHs in monoclinic Ga_2O_3 are holes trapped by an O atom in an O(III) site with a Ga neighbor and/or in an O(I) site distributed among two O sites.[26] The blue emission is attributed to recombination of an electron at a deep donor level and a hole at an acceptor level, or donor–acceptor pair (DAP). These donors are created by O vacancies (V_O), and acceptors are created by Ga (V_{Ga}) or Ga–O vacancy pairs (V_{Ga}–V_O)[29] and act as a hole trapping. These trapped holes lead to strong photoconductive gain, because multiple electron injections occur for each trapped

hole that was photogenerated by the UV illumination.[27] However, STHs are independent of impurities and diminish with increasing growth/annealing temperature.[30] We have further explored this temperature dependency of STH by annealing in terms of spectral responsivity variation of PD as described in the following section (Section 3.5.5). The green emission in CL spectra often attributed to the presence of specific impurities, such as Sn, Si, and Ge,[23] and this shallow donor levels may increase the conductivity of the film. Finally, the red/near IR luminescence is also attributed to impurities, attributed mainly to nitrogen doping,[23,25] or due to rare earth and transition metal impurities.[31] However, N_2 free growth in our MBE chamber indicates that it could be hydrogen atoms, which can provide an electron to form O—H bond by passivating an acceptor such as V_{Ga} and absorb IR at vibrational mode.[32] It may also be related to ionic V_O at different sites of the lattice.[22] However, identifying the actual source requires more investigation and is not included in this study.

3.5. Electrical Characterization and Device Properties

3.5.1. Self-Powered PD

A vertical Schottky device fabricated from 1.6 sccm O_2 flow samples A1 and B1 did not show any measurable photoresponse under 240 nm illumination. They behaved identically to that of a pure Si PD, suggesting the lack of a Ga_2O_3 epilayer, as stated earlier (see Section 3.1.2). The dark and UV-illuminated characteristics of a fabricated vertical Schottky detector from the 2.0 sccm O_2 flow sample (B2) are shown in **Figure 7**a. The device demonstrated a high dark current, >1 μA at −2 V, and had limited discernable photoresponse under reverse bias due to the high dark current background. The high dark current is attributable to multiple dominant defects in Ga_2O_3 thin films, such as O vacancies (V_O), neutral Ga interstitials, Ga vacancies, and Ga–O divacancies.[22,26,27] However, strong photoresponse at zero applied bias, a characteristic of self-powered devices, was observable, because the dark current under zero bias is only on the order of ≈1 pA, three orders of magnitude below the measured UV photocurrent of 4 nA. As shown in the inset of Figure 7a, the temporal response of the sample under self-powered conditions is very fast, with the rise and fall times below the 4 ms time resolution of our system. Very similar characteristics were observed for all 2.0 sccm samples, irrespective of substrate orientation.

Figure 7b provides the self-powered spectral responsivity of sample B2, demonstrating a 10% cutoff of about 260 nm, supporting the presence of a Ga_2O_3 film on Si substrate, and fulfilling the requirements of solar-blind detection. The other 2.0 and 2.5 sccm samples showed similar spectral responsivity characteristics. **Figure 8** provides a summary of the measured self-powered responsivities of the various devices at 0 V bias for (111) and (100) substrates under 240 nm illumination. Devices fabricated from the 2.0 and 2.5 sccm samples had self-powered responsivities ranging from 40 to 92 mA W^{-1} under zero bias, with (111)-based devices having ≈30% higher responsivity in comparison with (100)-based devices. We also find that 2.5 sccm flow devices led to higher self-powered responsivities over 2.0 sccm devices, irrespective of substrate orientation. We
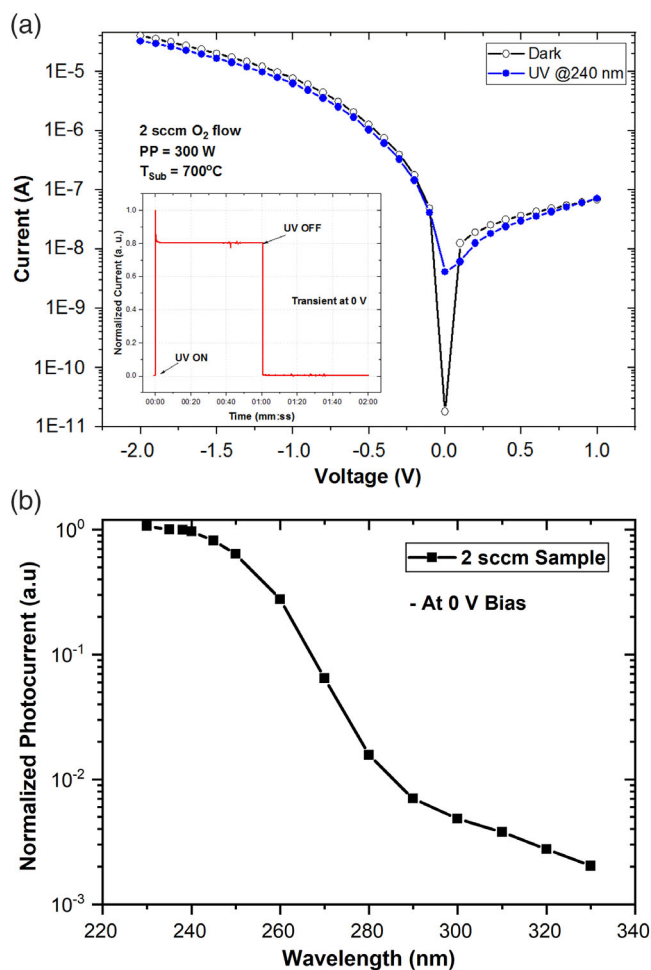
Figure 7. a) Dark and UV-illuminated *I–V* curve of a self-powered PD (sample B2). Inset shows the transient characteristics of the device at zero bias. b) The spectral responsivity of B2 in log scale shows nearly 10^3 times photocurrent enhancement with sharper cutoff below UV-C regime.
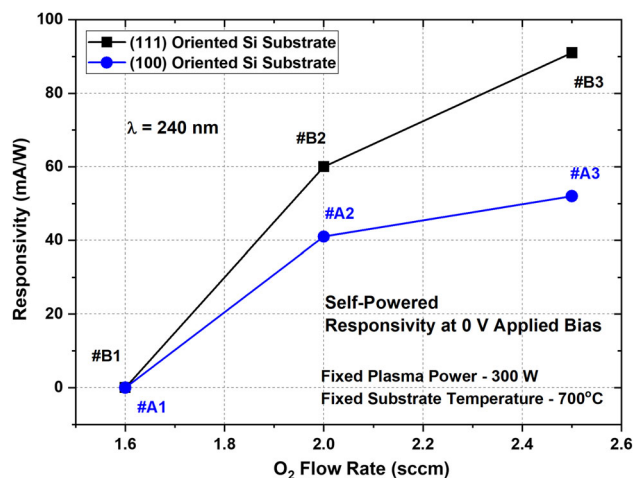
Figure 8. Peak responsivity values with different oxygen flow rate. Here, zero responsivity indicates that no UV photoresponse was measured, and the samples had Si PD characteristics.

**ADVANCED
SCIENCE NEWS**
www.advancedsciencenews.com

**ADVANCED
PHOTONICS
RESEARCH**
Open Access
www.adpr-journal.com

attribute this to improved growth at the nucleation, thus, a smoother interface, ideal for a vertical device.

3.5.2. Role of Si Substrate Orientation

As demonstrated earlier in Figure 3, the XRD ω–2θ peaks are identical for both the Si substrate orientation for all different oxygen flow rate. Furthermore, we observed the device performance on our fabricated structures, and based on our results, we agree with the observation of Berencén et al.[8] that crystallographic orientation of the silicon substrate plays no significant role in the ultimate properties of the Ga_2O_3 films. However, as noted earlier, we find that Schottky PDs on (111) Si show slightly better ($\approx$30%) responsivity in comparison with those on (100) Si. This may be attributed to the superior interfacial properties between Ga_2O_3 and (111)-oriented silicon substrate since (111)-oriented face of Si, which is more favorable for non-cubic crystal structure growth. Based on these findings, we then fixed the oxygen flow to 2.5 sccm and substrate orientation of (111) for the remaining samples used in this study. All the 2.5 sccm samples show an average of 40.3% Ga and 59.7% of oxygen estimated from the WDS measurement.

3.5.3. I–V Characteristics under Dark and UV Illumination

Fabricated vertical Schottky devices from all 2.5 sccm samples show clear rectifying behavior with measurable photocurrent generation in the reverse bias condition that is typically two orders of magnitude above the dark current. **Figure 9** shows the comparative dark and UV-illuminated I–V characteristics from the devices fabricated on samples C1, C1A, B3, and B4. These plots focus the incremental substrate temperature effects under the same plasma power of 300 W and discussed in detail in Section 3.5.5 and 3.5.6. I–V characteristics in Figure 9 have a slight shift ($\approx$−0.3 V) of current minima in the dark state, which possibly attributed to the charge trapping and de-trapping at the metal/Ga_2O_3 interface, a well-known phenomenon for Ga_2O_3.[33] Our PDs have Schottky contacts at the front side and ohmic at the backside. When PDs are under the forward bias or UV illumination, before measuring the dark current, the holes may trap near the Schottky junction via self-trapping[33] and or at deep level acceptor states. This may be the reason why we observe the shift in the I–V measurements for some devices, because the density of deep level acceptor levels is not the same for all the samples.

Normalized spectral responsivity measurements for those same devices are shown in **Figure 10**. The 700 and 730 °C
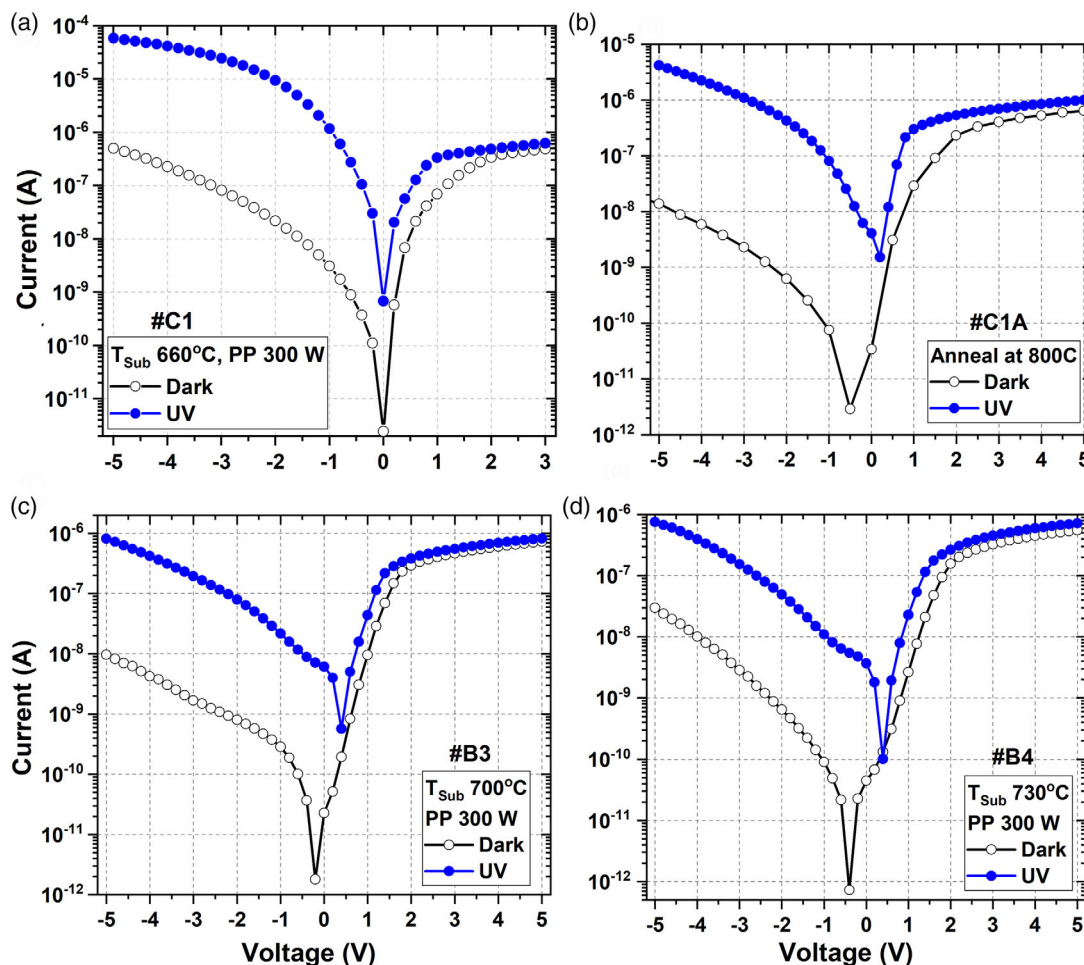
Figure 9. Comparative dark and photocurrent I–V characteristics for samples with different T_{sub}.

**ADVANCED
SCIENCE NEWS**

www.advancedsciencenews.com

**ADVANCED
PHOTONICS
RESEARCH**
Open Access

www.adpr-journal.com
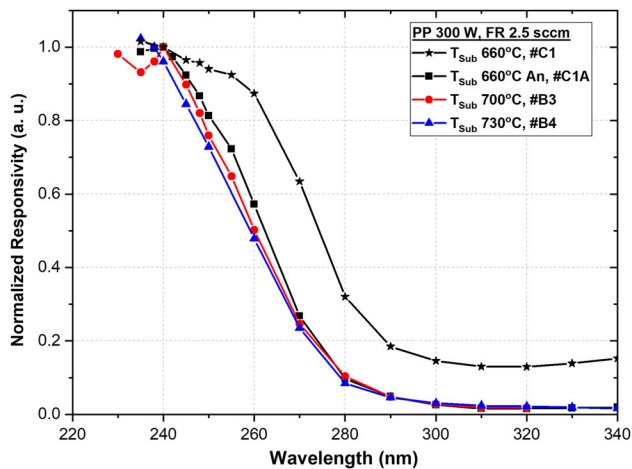
Figure 10. Normalized comparative responsivity at −5 V bias plotted with varying wavelength under various T_{sub}. A clear trend of sharper profile can be seen with increasing substrate temperature at fixed plasma power and O_2 flow rate.

samples (B3 and B4) have very similar spectral responsivity characteristics, showing a cutoff wavelength below 280 nm. In contrast, the 660 °C sample (C1) showed a longer wavelength cutoff, attributed to defects within the epilayers that create mid-gap states. Finally, peak responsivity of all the samples has been calculated by dividing mean current between I_{UV} and I_{Dark} with an incident optical power density at 248 nm, as shown in Table 1 and **Figure 11**.

3.5.4. Photoconductive Gain

The peak responsivity of the 660 °C sample (C1) is 837 A W^{-1} and at −5 V under 248 nm UV illumination, as shown in Figure 11. The peak responsivity value corresponds to an external quantum efficiency (EQE) greater than unity, suggesting
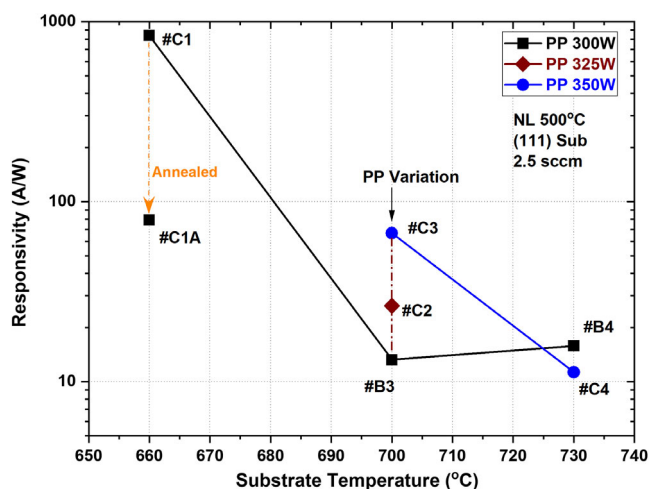
Figure 11. Peak responsivity values of different samples at −5 V bias with varying substrate temperature. Annealing effect as well as responsivity variation with applied plasma power also indicated. All the measurement were performed under 248 nm UV illumination from monochromator.

strong photoconductive gain is present. We, therefore, consider the gain-efficiency product as a more accurate metric of assessment for these devices than EQE alone.[28] Using the relation between the gain-efficiency product ($G \cdot \eta_{ext}$) and the device responsivity (R)

$$G \cdot \eta_{Ext} = \left(\frac{R \cdot h\nu}{q} \right) = \left[\frac{(I_{ph} - I_{dark}) \cdot h\nu}{q \cdot P_\lambda \cdot A} \right] \qquad (1)$$

where R is the responsivity at photon energy ($h\nu$), q is the electron charge, I_{ph} is the photocurrent when illuminated by light of energy $h\nu$, I_{dark} is the dark current, P_λ is the power density of the light on the device with photon energy $h\nu$, and A is the device area, yielding gain-efficiency products on the order of hundreds. Given the gain-efficiency product, the values are greater than 1.0, indicating that the devices have a significant gain, G. From our previous experience, we have seen that Ga_2O_3 and its ternary alloys are prone to bulk and surface defects that lead to photoconductive gain,[1,28,34] particularly when grown on lattice mismatched Si substrates. In Section 3.4, CL study of our samples shows evidence for mid-bandgap donor/acceptor defects, which lead to the photoconductive gain. STHs, the UV and blue band emission in Figure 6, are the major contributor in PD gain, attributed to the recombination of electrons with the trapped holes. However, STHs diminish with increasing growth/anneal temperature. Experimental results are as follows in the next section.

3.5.5. Effects of Annealing

To investigate the effects of temperature on STH characteristics, a separate piece of the low T_{sub} (660 °C) grown sample (sample C1) was annealed at 800 °C under vacuum for 4 h (sample C1A). A slight thickness reduction (≈10%) has been observed by profilometry, potentially due to some limited dissociation and desorption of Ga_2O_3. Similar thickness reduction has also been observed due to annealing in the case of indium gallium oxide.[35] The XRD pattern from the as-grown and annealed samples was identical, indicating that no measurable change in the crystal structure of the film occurred during the vacuum anneal. Figure 10 includes the comparative spectral responsivity measurements from detectors fabricated from both samples. The annealed sample (C1A) exhibits a sharper spectral response cutoff characteristic that is accompanied by a ≈12 nm blue shift to shorter wavelength, moving from 260 to 248 nm. Experimental results indicate that this is related to a reduction in defect-related energy levels associated with mainly STH, prominent at low T_{sub}, that are reduced through the annealing process. We observe a nearly two order of magnitude drop in dark current for the annealed sample, from 500 to 10 nA at −5 V, as shown in Figure 9a,b, supporting the conclusion that the density of defects in the devices has been reduced on annealing. This reduction in defects leads to a reduction in the number of STHs, thus reducing photoconductive gain and measured responsivity in the vertical Schottky devices. Peak responsivity of the annealed sample (C1A) was found to be 79 A W^{-1}, whereas the peak responsivity of the original as-grown sample (C1) was 837 A W^{-1} at −5 V under 248 nm UV illumination, as shown in Figure 11. Following the trend, the detectivity of C1A also decreases,
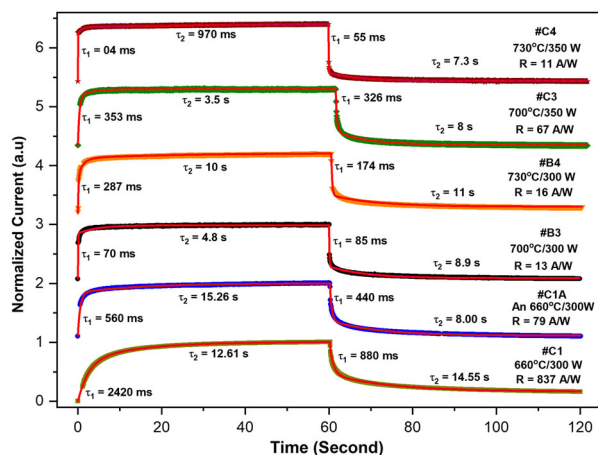
Figure 12. Normalized transient characteristics with values of rise/fall times of different samples with varying T_{sub} and plasma power. Symbols are the actual data points, whereas the red color straight line is double exponential fittings using equation $I(t) = I_0 + Ae^{-(t-t_0)/\tau_1} + Be^{-(t-t_0)/\tau_2}$ as described in the previous study.[28]

however, only half-order from 2.8×10^{11} cm.$\sqrt{Hz}$/W of C1, due to the lower dark current, as shown in Table 1 and Figure S3, Supporting Information. The reduction in photoconductive gain also led to faster transient characteristics for the annealed sample (C1A). The measured rise and fall times (τ_1) of devices from the annealed sample, determined from a double exponential fit, were 540 and 440 ms, respectively, whereas those from the as-grown original sample (C1) were 2.4 s and 880 ms, respectively, as shown in **Figure 12**.

Despite the reduction in measured peak responsivity, it is still high after annealing, indicating that photoconductive gain is still present. This suggests that annealing reduces the density of defects in the epilayers but many still remain, likely due to being annealed under vacuum rather than under the oxygen overpressure from the O-plasma that would reduce oxygen vacancies. Therefore, we further experimented with growth at higher T_{sub} under oxygen overpressure, as described in the next section (Section 3.5.6) and studied its relation with densities of possible donor/acceptor levels detected by CL (see Section 3.5.8).

3.5.6. Effect of High Growth Temperature

Figure 12 provides the temporal characteristics of several devices fabricated from samples grown under various T_{sub}. Rise and fall times determined from each using a double exponential fit[28] are listed in Table 1. The data demonstrate that growth at higher substrate temperatures can lead to better temporal response as long as the proper plasma power is selected. Moving from a T_{sub} of 660 to 700 °C results in shorter τ_1 time; however, increasing T_{sub} further to 730 °C results in a minor increase in transient, but still well below those of the 660 °C samples. This can be compensated by increasing the plasma power to 350 W, leading to the fastest observed response time. Such a trend is expected given that we observe lower responsivity and photoconductive gain for higher substrate temperatures, accompanied by lower defect densities due to growth in less metal-rich conditions. This, in turn, leads

to faster response times in the resultant devices. Moreover, devices do not show any photo-persistent (PPC) effects. Figure S4, Supporting Information, with multiple cycle transient data in supplementary document shows the absence of PPC. It also shows the robustness of our fabricated Ga_2O_3 devices, because the consistent repeating transient cycles shown in Figure S4, Supporting Information, were measured after 2 years from fabrication of the samples.

3.5.7. Impact of Oxygen Plasma Power

To determine the impact of oxygen plasma power on device characteristics, we carried out a sequence of growths at the plasma powers of 300, 325, and 350 W (samples B3, C2, and C3) under a fixed T_{sub} of 700 °C and 2.5 sccm oxygen flow. Figure 11 shows that the peak responsivity increases with increasing plasma power at a constant T_{sub} of 700 °C, increasing from 13.2 A W^{-1} at 300 W to a value of 66.8 A W^{-1} at 350 W. Similarly, detectivity also increases from 3 to 8.84×10^{10} Jones, as shown in Figure S3, Supporting Information. Increased RF plasma power might decrease the oxygen vacancies while it may also increase the gallium vacancies and unintentional doping (discussed in next paragraph). The dominant presence of Ga vacancies contributes significantly to the photoconductive gain. The shoulder in the blue band at an emission energy of 2.7 eV (see Figure 6) may be associated with V_{Ga} defects and a lower formation energy of divacancies[22] that can trap holes dominantly at ($V_{Ga} + V_O$). At moderate growth temperatures, shifting of the growth conditions toward oxygen-rich conditions decreases the formation energy of defects that are expected to become the majority hole trap. This is reflected in **Figure 13** where increasing plasma power increases blue band emission intensity related to V_{Ga} defects and DAP divacancy transitions involving deep donor and acceptors.[36] These mid-bandgap levels increase photoconductive gain considerably, as explained earlier. Thus, as expected, for a fixed 700 °C T_{sub}, device responsivity increases as plasma power is increased from 300 to 350 W, as shown in Figure 11 and 13c, among samples B3, C2, and C3.

We find two contrasting trends for samples grown at a T_{sub} of 730 °C, with the 350 W sample (C4) having a slightly reduced peak responsivity in comparison with the 300 W sample (B4), dropping from 15.8 to 11.3 A W^{-1} and faster transient behavior. As explained earlier, point defect densities related to UV/blue emission band decrease at higher growth temperature, thus reducing responsivity at high T_{sub} as well as promoting faster transient characteristics. However, unintentional impurities in Ga_2O_3, most likely H and Si, become dominant, especially under higher oxygen partial pressure in the growth atmosphere in the case of undoped crystals.[23] Hydrogen can easily occupy either interstitial or substitutional sites due to its low formation energy[27,37] during MBE growth and is present due to hydrocarbon and water cleaning of the Si substrate. Moreover, it is expected that the Ga_2O_3 layer in the vicinity of the Si substrate would be unintentionally doped by Si, preferring the tetrahedral coordination of the Ga(I) site.[38] Therefore, interstitial H and substitutional Si create a shallow donor level within the bandgap of monoclinic Ga_2O_3[39] and contribute significantly to the n-type conductivity of Ga_2O_3. The green emission in the CL spectra, as shown in Figure 6, is often attributed to the presence of

**ADVANCED
SCIENCE NEWS**

www.advancedsciencenews.com

**ADVANCED
PHOTONICS
RESEARCH**
Open Access

www.adpr-journal.com
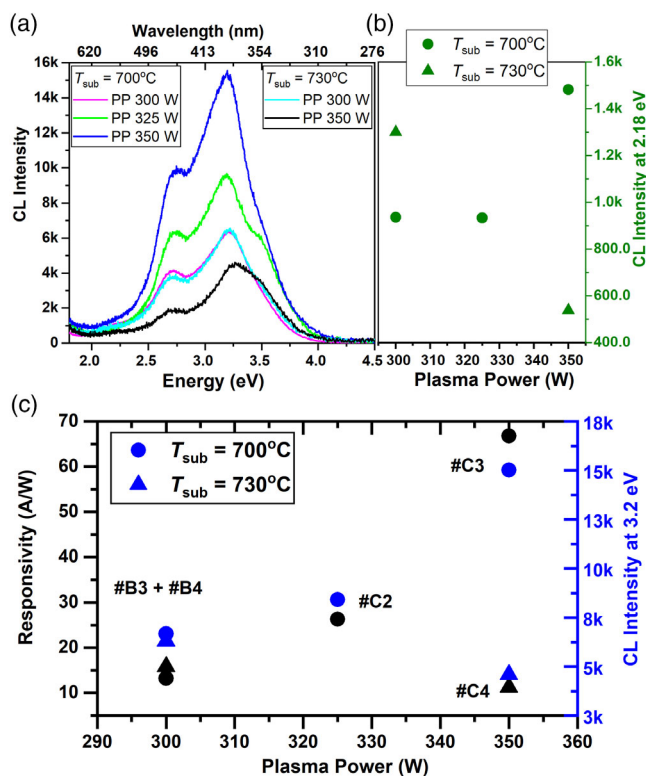
Figure 13. Comparative a) CL spectrum, b) CL peak intensity at 2.18 eV, and c) PD response against CL peak intensity at 3.2 eV for samples B3, B4, C2, C3, and C4 on varying the plasma power.

impurities, and its intensity decreases with increasing conductivity. We have observed the lowest green band intensity for sample C4 (highest T_{sub} of 730 °C and 350 W plasma power), as shown in Figure 13b, leading to the fastest transient characteristics, as shown in Figure 12.

3.5.8. Impact of Point Defects on Device Response

Direct evidence of growth temperature impact on defect density is seen in comparative CL intensities, as shown in Figure 13a. It is reasonable to compare the CL peak intensity with our

collection optics, and the excitation volume averages out any minor variation in the peak intensity due to the polycrystalline nature of the samples. CL intensity represents the density of donor/acceptor levels at corresponding possible mid-bandgap positions. Therefore, reduction in the peak intensity of UV and blue emission with increasing growth temperature (under fixed plasma power) qualitatively shows reduction of STH density and photoconductive gain associated with it, as shown in Figure 13c. A closer look at Figure 10 also shows blue shift of spectral responsivity with increasing growth temperature, associated with decreasing mid-bandgap defect levels. We note that devices from the 730 °C T_{sub} sample (sample C4) were found to have very similar peak responsivity, rise/fall times, and CL intensity as those from the 700 °C sample, suggesting that above 700 °C, we may have saturated the benefit in improved deep donor/acceptor levels density for higher T_{sub}. However, a more detailed study with more data points would be necessary to better determine this trend, but, qualitatively, we find that higher T_{sub} leads to faster devices with reduced peak responsivity.

While analyzing the rise and fall times of 700 °C for samples B3, C2, and C3 (see Table 1), we can see that higher plasma power causes a measurable increase in the τ_1 and τ_2 of the devices, while increasing responsivity and detectivity. This suggests that while a higher plasma power at 700 °C T_{sub} improves responsivity, it promotes hole trapping by incorporation of V_{Ga} and divacancy defects that degrade the temporal characteristics of the devices slightly. In contrast, samples grown at 730 °C T_{sub} exhibit an opposite trend, with the 300 W sample (B4) having roughly an order of magnitude longer τ_1 and τ_2 in comparison with the 350 W sample (C4) mainly due to increase in conductivity by unintentional impurities. Despite the very similar peak responsivity measured for the two samples, the higher plasma power sample at 730 °C T_{sub} appears to have superior temporal characteristics without a measurable penalty in responsivity and detectivity.

We have compared our device characteristic results (see **Table 2**) with the results obtained from the previous work reported in the literature particularly on PDs fabricated on Si. There are very few reports on PDs using Ga_2O_3 on Si substrates. Among those results, our PDs demonstrate significantly superior characteristics in almost all figures-of-merit. We have further compared results with solar-blind Ga_2O_3 PDs grown on sapphire and Ga_2O_3. The comparative results show that our device

Table 2. Comparative table of PD characteristics with published data.

Material	Device	Method	Detection wavelength [nm]	I_{dark}	Reject. ratio	Responsivity	Rise/fall time	Ref.
Ga_2O_3/sapphire	MSM	MBE	254	1.4 nA@10 V	77	0.037 A W^{-1}	–	[40]
Ga_2O_3/SiC	Heterojunction	PLD	254	500 pA	–	0.18 A W^{-1}	0.65 s rise/1.73 s fall	[41]
Ga_2O_3	Schottky	MBE, homoepitaxy	200–260	10 nA	1000@3 V	2.6–8.7 A W^{-1}	–	[42]
Ga_2O_3/p-Si	Schottky	PLD	254	30 nA@−3 V	–	370 A W^{-1}	1.79 s rise/2.72 s fall	[6]
Ga_2O_3/Si	MSM	Seed layer	254	1.43 pA@0 V	1000	96.13 A W^{-1}@5 V	32 ms rise/78 ms fall	[9]
Ga_2O_3/p-Si	p–n junction	Exfoliation	254	70 nA@35 V	15 600	–	4.06 s rise/0.16 s fall	[10]
Ga_2O_3/n-Si	Schottky	MBE	245–260	0.9 pA@0 V; 9 nA@−5 V	1000@0 V; 400@−5 V	837 A W^{-1}@−5 V; 11 A W^{-1}@−5 V	2.4 s rise/0.88 s fall; 4 ms rise/55 ms fall	This work

**ADVANCED
SCIENCE NEWS**

www.advancedsciencenews.com

**ADVANCED
PHOTONICS
RESEARCH**
Open Access

www.adpr-journal.com

characteristics are comparable and, in some cases, outperform those results, providing a cost-effective platform on which on-wafer integration with Si photonics would be possible.

4. Summary and Conclusion

This work represents the first systematic study of the impact of key growth conditions on the nucleation and growth of Ga_2O_3 on lattice mismatched Si substrates by PAMBE to the fabricated devices. Growth temperature, oxygen flow, and plasma power were found to have significant impact on the resultant epilayers and characteristics of vertical Schottky photodiodes fabricated from the Ga_2O_3/n-Si heterostructures. Adequate Ga pre-deposition is necessary to realize proper nucleation and growth of Ga_2O_3 films on Si, primarily due to the suppression of SiO_2 formation, as verified by XPS. Nevertheless, growth under sufficient Ga flux but lower oxygen supply favors the formation of volatile Ga sub-oxides, which also promote SiO_2 formation, thereby suppressing the Ga_2O_3 film growth. As a result, the minimum oxygen flow rates of 2.0 sccm have been identified as sufficient for nucleation and growth of Ga_2O_3. Detectors fabricated under such a growth condition produced dark currents in the μA regime, limited the detector to operate in the self-powered mode where photogenerated current exceeded dark currents under zero bias. Growth under a higher oxygen flow rate of 2.5 sccm led to growth of β-Ga_2O_3 under less metal-rich conditions, enabling Schottky devices with strong responsivities, as high as $837\,A\,W^{-1}$, under reverse bias conditions. Adjusting the growth conditions gives control over photoconductive gain due to change in mid-bandgap defect levels including oxygen vacancies in the form of STHs. Annealing as well as higher growth temperature led to lower photoconductive gain and peak responsivity ($\approx 10\,A\,W^{-1}$) with improved temporal response in the millisecond regime. At a fixed substrate temperature ($700\,^\circ C$), higher oxygen plasma power led to a measurable increase in device responsivity, from $13.2\,A\,W^{-1}$ at 300 W to $66.8\,A\,W^{-1}$ at 350 W but was accompanied by a worsening in the temporal characteristics of the devices. The PDs fabricated from epilayers grown at high plasma power and growth temperature had the fastest response, with detectivity following the trend of responsivity. The Si substrate orientation was not found to have an impact on the β-Ga_2O_3 epilayers orientation, as well as on their device characteristics. This work provides valuable insight into the proper nucleation and growth of Ga_2O_3 on n-type-doped Si substrates. It further demonstrates the viability of functional Ga_2O_3/Si UV-C solar-blind detectors that are competitive with homoepitaxial approaches, identifying how growth conditions can be selected to adjust the responsivity, detectivity, and temporal characteristics by means of controlling defect related mid-bandgap donor levels.

Supporting Information

Supporting Information is available from the Wiley Online Library or from the author.

Conflict of Interest

The authors declare no conflict of interest.

[1] P. Mukhopadhyay, W. V. Schoenfeld, *Appl. Opt.* **2019**, *58*, D22.
[2] S. J. Pearton, J. Yang, P. H. Cary, F. Ren, J. Kim, M. J. Tadjer, M. A. Mastro, *Appl. Phys. Rev.* **2018**, *5*, 011301.
[3] M. Toporkov, P. Mukhopadhyay, H. Ali, V. Beletsky, F. Alema, A. Osinsky, W. V. Schoenfeld, *Devices VIII* **2017**, *10105*, 101051N.
[4] S. D. Wolter, B. P. Luther, D. L. Waltemyer, C. Önneby, S. E. Mohney, R. J. Molnar, *Appl. Phys. Lett.* **1997**, *70*, 2156.
[5] S. Nakagomi, T. Momo, S. Takahashi, Y. Kokubun, *Appl. Phys. Lett.* **2013**, *103*, 072105.
[6] X. C. Guo, N. H. Hao, D. Y. Guo, Z. P. Wu, Y. H. An, X. L. Chu, L. H. Li, P. G. Li, M. Lei, W. H. Tang, *J. Alloys Compd.* **2016**, *660*, 136.
[7] Z. Chen, K. Nishihagi, X. Wang, K. Saito, T. Tanaka, M. Nishio, M. Arita, Q. Guo, *Appl. Phys. Lett.* **2016**, *109*, 1.
[8] Y. Berencén, Y. Xie, M. Wang, S. Prucnal, L. Rebohle, S. Zhou, *Semicond. Sci. Technol.* **2019**, *34*, 035001.
[9] K. Arora, N. Goel, M. Kumar, M. Kumar, *ACS Photonics* **2018**, *5*, 2391.
[10] G. Shin, H. Y. Kim, J. Kim, *Korean J. Chem. Eng.* **2018**, *35*, 574.
[11] H. Altuntas, I. Donmez, C. Ozgit-Akgun, N. Biyikli, *J. Vac. Sci. Technol. A Vac. Surf. Film* **2014**, *32*, 041504.
[12] J. T. Gibbon, L. Jones, J. W. Roberts, M. Althobaiti, P. R. Chalker, I. Z. Mitrovic, V. R. Dhanak, *AIP Adv.* **2018**, *8*, 8.
[13] M. K. Yadav, A. Mondal, S. Das, S. K. Sharma, A. Bag, *J. Alloys Compd.* **2020**, *819*, 153052.
[14] A. Mahmoodinezhad, C. Janowitz, F. Naumann, P. Plate, H. Gargouri, K. Henkel, D. Schmeißer, J. I. Flege, *J. Vac. Sci. Technol. A* **2020**, *38*, 022404.
[15] H. W. Kim, N. H. Kim, C. Lee, *J. Mater. Sci.* **2004**, *39*, 3461.
[16] P. Mukhopadhyay, S. Chowdhury, A. Wowchak, A. Dabiran, P. Chow, D. Biswas, *J. Vac. Sci. Technol. B* **2013**, *31*, 03C132.
[17] P. Mukhopadhyay, W. V. Schoenfeld, in *3rd Int. Work. Gall. Oxide Relat. Mater. (IWGO-3)*, MRS, Materials Research Society, Philadelphia, USA **2019**.
[18] P. Mukhopadhyay, R. Kumar, S. Ghosh, A. Chakraborty, A. Bag, S. Kabi, P. Banerji, D. Biswas, *J. Cryst. Growth* **2015**, *418*, 138.
[19] H.-Y. Shih, F.-C. Chu, A. Das, C.-Y. Lee, M.-J. Chen, R.-M. Lin, *Nanoscale Res. Lett.* **2016**, *11*, 235.
[20] P. Vogt, O. Bierwagen, *Appl. Phys. Lett.* **2016**, *108*, 072101.
[21] P. Vogt, O. Bierwagen, *Appl. Phys. Lett.* **2015**, *106*, 081910.
[22] Q. D. Ho, T. Frauenheim, P. Deák, *Phys. Rev. B* **2018**, *97*, 1.

[23] K. Shimamura, E. G. Víllora, T. Ujiie, K. Aoki, *Appl. Phys. Lett.* **2008**, *92*, 201914.

[24] H. Gao, S. Muralidharan, N. Pronin, M. R. Karim, S. M. White, T. Asel, G. Foster, S. Krishnamoorthy, S. Rajan, L. R. Cao, M. Higashiwaki, H. Von Wenckstern, M. Grundmann, H. Zhao, D. C. Look, L. J. Brillson, *Appl. Phys. Lett.* **2018**, *112*, 1.

[25] G. Pozina, M. Forsberg, M. A. Kaliteevski, C. Hemmingsson, *Sci. Rep.* **2017**, *7*, 42132.

[26] T. Gake, Y. Kumagai, F. Oba, *Phys. Rev. Mater.* **2019**, *3*, 44603.

[27] J. B. Varley, J. R. Weber, A. Janotti, C. G. Van De Walle, *Appl. Phys. Lett.* **2018**, *97*, 142106.

[28] P. Mukhopadhyay, W. V. Schoenfeld, *J. Vac. Sci. Technol. A* **2020**, *38*, 013403.

[29] L. Binet, D. Gourier, *J. Phys. Chem. Solids* **1998**, *59*, 1241.

[30] A. I. Kuznetsov, V. N. Abramov, T. V. Uibo, *Opt. Spectrocopy* **1985**, *58*, 368.

[31] G. Naresh-Kumar, H. Macintyre, S. Shanthi, P. R. Edwards, R. W. Martin, K. Daivasigamani, K. Sasaki, A. Kuramata, *Phys. Status Solidi B* **2020**, 2000465.

[32] M. D. McCluskey, *J. Appl. Phys.* **2020**, *127*, 101101.

[33] Y. K. Frodason, K. M. Johansen, L. Vines, J. B. Varley, *J. Appl. Phys.* **2020**, *127*, 075701.

[34] I. Hatipoglu, P. Mukhopadhyay, F. Alema, T. S. Sakthivel, S. Seal, A. Osinsky, W. V. Schoenfeld, *J. Phys. D. Appl. Phys.* **2020**, *53*, 454001.

[35] F. Zhang, H. Jan, K. Saito, T. Tanaka, M. Nishio, T. Nagaoka, M. Arita, Q. Guo, *Thin Solid Films* **2015**, *578*, 1.

[36] T. Onuma, S. Fujioka, T. Yamaguchi, M. Higashiwaki, K. Sasaki, T. Masui, T. Honda, *Appl. Phys. Lett.* **2013**, *103*, 041910.

[37] A. Janotti, C. G. Van De Walle, *Nat. Mater.* **2007**, *6*, 44.

[38] E. G. Víllora, K. Shimamura, Y. Yoshikawa, T. Ujiie, K. Aoki, *Appl. Phys. Lett.* **2018**, *92*, 202120.

[39] P. D. C. King, I. McKenzie, T. D. Veal, *Appl. Phys. Lett.* **2010**, *96*, 1.

[40] T. Oshima, T. Okuno, S. Fujita, *Jpn. J. Appl. Phys.* **2007**, *46*, 11.

[41] Y. Qu, Z. Wu, M. Ai, D. Guo, Y. An, H. Yang, L. Li, W. Tang, *J. Alloys Compd.* **2016**, *680*, 247.

[42] T. Oshima, T. Okuno, N. Arai, N. Suzuki, S. Ohira, S. Fujita, *Appl. Phys. Express* **2008**, *1*, 011202.